



Homogeneous ice nucleation in adsorbed water films: A theoretical approach

Ari Laaksonen^{1,2}, Golnaz Roudsari¹, Ana A. Piedehierro¹, and André Welti¹

¹Finnish Meteorological Institute, FI-00101 Helsinki, Finland

²Department of Technical Physics, University of Eastern Finland, 70211 Kuopio, Finland

Correspondence: Ari Laaksonen (ari.laaksonen@fmi.fi)

Abstract. Ice nucleation plays a critical role in cloud formation and atmospheric processes, influencing precipitation and climate. In this study, we present a theoretical approach for describing homogeneous ice nucleation within adsorbed water films on insoluble substrates, and suggest that it may be a mechanism for deposition ice nucleation with non-porous ice nuclei that induce ice premelting. Our theory is based on the Frenkel-Halsey-Hill (FHH) adsorption model, which characterizes the substrate-adsorbate interaction, and the classical nucleation theory of homogeneous freezing, which describes the probability of ice formation. We use the theory to model the melting point, critical ice nucleus size, and nucleation rates as functions of adsorbed water film thickness and substrate properties. Our results indicate that the melting point depression can be as much as 5 K on hydrophilic substrates when the thickness of the water film is 1 nm. The onset temperature for homogeneous ice nucleation (235 K for cloud droplets) can shift 1-2 K lower in adsorbed films. At temperatures below 235 K, the humidity at which ice nucleation occurs is determined by the condition that the adsorbed water film must be thick enough to accommodate the critical ice nucleus. Comparisons of calculated relative humidity conditions with experimental ice nucleation data for silica particles show promising agreement, validating the FHH model as a framework for describing deposition ice nucleation in the atmosphere.

1 Introduction

Atmospheric ice nucleation can occur via homogeneous or heterogeneous freezing of cloud droplets or aqueous aerosols, or via deposition of water vapor onto surfaces of solid, insoluble ice nuclei (Pruppacher and Klett, 1997). Despite its importance for the evolution of clouds and precipitation, many aspects of ice nucleation processes remain poorly understood even after a century of research (Laaksonen and Malila, 2021). During the recent decade, the suggestion that ice nucleation from deposition may involve adsorption or pore condensation followed by a freezing mechanism (Welti et al., 2014; Marcolli, 2014) has led to the question of how the size of the system, for example, pore dimensions or film thickness, affects the homogeneous nucleation of supercooled water (Marcolli, 2020). In confined geometries, the chemical potential of water differs from that of bulk water. Furthermore, the critical ice nucleus must fit within the system dimensions. There have been conflicting molecular simulation results regarding ice nucleation in free-standing water films (that is, films in contact only with their own vapor) having thicknesses in the nanometer range, some studies finding increasing (Haji-Akbari and Debenedetti, 2017) and other



25 studies decreasing (Lü et al., 2013; Haji-Akbari et al., 2014) homogeneous nucleation rates with decreasing film thickness. Hayton et al. (2024) recently suggested that the discrepancies can be reconciled by accounting for the intermolecular potential truncation applied in the various studies. Their own simulations indicated that homogeneous ice nucleation remains bulk-like down to a film thickness of about 3.5 nm. In the atmosphere, water films do not exist as separate entities, but multilayer water films can adsorb on the surfaces of atmospheric aerosols at sufficiently high relative humidities.

30 Deposition ice nucleation was originally treated within the classical nucleation theory framework by Fletcher (1959) as vapor molecules depositing directly into the crystalline phase, without an intermediate liquid-like state. However, because of the much smaller critical radius of ice in liquid compared to in vapor, the formation of a critical ice nucleus is much more likely due to fluctuations in the supercooled liquid rather than an ensemble of vapor molecules depositing on a surface almost simultaneously and in such a configuration that they are immediately able to form a hexagonal crystal. From this perspective, freezing of adsorbed films on nonporous, insoluble aerosols would seem to be a more likely route to deposition ice nucleation than the direct vapor-to-ice mechanism. Indeed, our recent molecular dynamics simulations (Roudsari et al., 2024) have shown that a water film with a thickness of just four monolayers can freeze on silver iodide surfaces at a temperature of 253 K.

The Frenkel-Halsey-Hill (FHH) adsorption activation theory (Sorjamaa and Laaksonen, 2007) has been successfully used to describe the activation of cloud condensation nuclei (CCN) of various types of insoluble particles (Kumar et al., 2011). In this work, we use FHH theory as a framework to derive the chemical potentials of adsorbed water and ice and use them to describe the thermodynamics of ice nucleation in supercooled water films. Theoretical predictions are compared to laboratory measurements on ice nucleation induced by silica particles.

2 Theory

2.1 Film-wise adsorption

45 We model film-wise adsorption on insoluble substrates using the FHH theory (Frenkel, 1946; Halsey, 1948; Hill, 1952), which contains two parameters (A and B) that must be determined experimentally, either by measuring adsorption isotherms (Halsey, 1948; Laaksonen, 2015) or by measuring CCN activation (Kumar et al., 2011). These measurements are usually made at or close to room temperatures, whereas our aim is to derive a theory of the freezing of adsorbed films at temperatures tens of degrees below room temperature. We therefore start by considering the temperature dependence of film-wise multilayer adsorption, which can be derived starting from the Clausius-Clapeyron equation (see, e.g., Kanagy (1950)). At any constant number of adsorbed monolayers N , the difference of the logarithms of equilibrium saturation ratios S_1 and S_2 at temperatures T_1 and T_2 is

$$\ln S_2 - \ln S_1 = \frac{\Delta L_A}{k} \left(\frac{1}{T_1} - \frac{1}{T_2} \right), \quad (1)$$

where $\Delta L_A = L_A - L_V$ with L_A the heat of adsorption and L_V the heat of vaporization of liquid water, and k is the Boltzmann constant.



We model multilayer adsorption using the FHH adsorption isotherm. The isotherm can be written as

$$\ln S = -AN^{-B}, \quad (2)$$

where A and B are constants describing the molecular interaction between the first adsorbed monolayer and the adsorbent, and the rate of decay of the interaction as a function of film thickness, respectively. In previous work (Laaksonen et al., 2020), the temperature dependence of the isotherm was not considered, since the calculations have been done for room temperature. However, in the original form of the FHH isotherm, derived assuming the Lennard-Jones (LJ) intermolecular potential, the A parameter is in fact temperature dependent. With A depending on temperature, we can rewrite Eq. 2 in similar form as Eq. 1:

$$\ln S_2 - \ln S_1 = (A(T_1) - A(T_2))N^{-B} \quad (3)$$

We now assume the following specific T dependence for the parameter A :

$$A(T) = A'/(kT) \quad (4)$$

where A' is a temperature-independent constant. Inserting Eq. 4 into Eq. 3 we obtain

$$\ln S_2 - \ln S_1 = \left(\frac{A'}{k}\right) \left(\frac{1}{T_1} - \frac{1}{T_2}\right) N^{-B}. \quad (5)$$

Comparing Eq. 5 with Eq. 1, we have $A'N^{-B} = \Delta L_A$. From now on, when we assign values to the A parameter, they refer to $T = 298 \text{ K}$, and $A(T)$ at other temperatures is obtained according to Eq. 4.

When an adsorbed film forms on an aerosol particle, Eq. 2 alone is not sufficient to calculate the equilibrium saturation ratio. The curvature of the particle induces a Kelvin effect that increases the vapor pressure of the film. To account for the Kelvin effect, Eq. 1 can be extended (Sorjamaa and Laaksonen, 2007) to

$$\ln S = -AN^{-B} + \frac{2\gamma v}{kTR}, \quad (6)$$

where γ is the air-water surface tension, v is molecular volume of water, and R is radius from the center of the aerosol particle (assumed spherical) to the surface of the adsorbed film. Denoting the radius of the dry aerosol particle by R_p , the thickness of the film equals $R - R_p$ and the number of adsorbed monolayers

$$N = \frac{R - R_p}{d}, \quad (7)$$

with d the thickness of an adsorbed monolayer.

2.2 Freezing of bulk water

We treat the freezing of adsorbed water using the classical nucleation theory (CNT). The homogeneous nucleation rate of ice in bulk water is given by (Laaksonen and Malila, 2021)

$$J_{hom} = C \exp \frac{-16\pi v_i^2 \gamma_{iw}^3}{3kT \Delta \mu_{iw}^2}, \quad (8)$$



where C is a kinetic prefactor, v_i is molecular volume of ice, γ_{iw} is the interfacial tension between water and ice, and $\Delta\mu_{iw}$ denotes the chemical potential difference between ice and water. The radius of the critical ice nucleus in water is given by

$$85 \quad R_{iw}^* = \frac{2v_i\gamma_{iw}}{\Delta\mu_{iw}}. \quad (9)$$

The chemical potential difference is usually approximated by

$$\Delta\mu_{iw} \approx kT \ln \left(\frac{e_w}{e_i} \right), \quad (10)$$

where the e 's denote the equilibrium vapor pressures of bulk water and ice, respectively.

2.3 Chemical potential of adsorbed water

90 When the mother phase of nucleating ice is adsorbed water instead of bulk water, the chemical potential of the liquid phase is equal to that of its equilibrium vapor having pressure P and saturation ratio over ice $S_i = P/e_i$, and the chemical potential difference between bulk ice and adsorbed liquid can be expressed as

$$\Delta\mu_{ia} \approx kT \ln S_i. \quad (11)$$

If bulk ice is taken to be the stable state, then freezing should not occur at $P < e_i$. However, adsorbed ice films obviously
95 can exist at subsaturation (just as adsorbed water films can exist at relative humidity below 100%), and a transition from a supercooled liquid film to an ice film through nucleation must be possible when the temperature is below the melting point of the ice film, even if the pressure of the vapor in equilibrium with the film is below e_i .

We postulate that the stable reference state for a supercooled liquid film containing a given number of water molecules at temperature T is, instead of bulk ice, a film consisting of hexagonal ice that has the same number of molecules as the water film.

100 The chemical potential difference between liquid and ice films with fixed number of water molecules n_{H_2O} can be expressed by the FHH theory. The equilibrium for a liquid film is given by

$$\ln \frac{P_w}{e_w} = -A_w N_w^{-B_w}. \quad (12)$$

Here P_w is the pressure of water vapor in equilibrium with the adsorbed film. For the ice film, we write

$$\ln \frac{P_i}{e_i} = -A_i N_i^{-B_i}. \quad (13)$$

105 Now,

$$n_{H_2O} = \Omega N_w \frac{d_w}{v_w} = \Omega N_i \frac{d_i}{v_i}, \quad (14)$$

where Ω is the surface area covered by the film, and the v 's and d 's are the molecular volumes and monolayer thicknesses, respectively, of water and ice. Thus,

$$N_i = \left(\frac{\sigma_i}{\sigma_w} \right) N_w \quad (15)$$



110 with σ' s denoting the cross sections of water and ice on the surface of the adsorbent ($\sigma = v/d$). The monolayer thickness
of water is taken to be $d_w = 2.84 \text{ \AA}$, which corresponds to a cross section of $\sigma_w = 10.5 \text{ \AA}^2$ (McClellan and Harnsberger,
1967). For the monolayer thickness of ice, we use half of the intermolecular distance along the vertical direction (c-axis) of the
hexagonal unit cell from molecular dynamics simulations, $d_i = 3.63 \text{ \AA}$ (Roudsari et al., 2024), which is in good agreement with
temperature-dependent lattice parameter measurements from neutron diffraction (Fortes, 2018). Note that the cross-section of
115 ice $\sigma_i \approx 8.9 \text{ \AA}^2$ is smaller than σ_w .

Using Eqs. 12 and 13 to express the equilibrium vapor pressure wrt. water and ice, the chemical potential difference between
the adsorbed liquid and ice films can be written as

$$\Delta\mu_A \approx kT \ln \frac{P_w}{P_i} = kT \left[\ln \frac{e_w}{e_i} + A_i N_i^{-B_i} - A_w N_w^{-B_w} \right]. \quad (16)$$

The vapor pressures of the liquid and the ice films are equal at the melting point of the ice film, which can therefore be found
120 by locating the temperature at which $\Delta\mu_A = 0$ (see Figs. 4 & 5). We note that for this requirement to be fulfilled, the sum of
the last two terms on the right-hand side of the above equation must be negative. This imposes restrictions on the values that the
set of FHH parameters (A_i, A_w, B_i, B_w) can have. For example, because the FHH parameters describe molecular interactions
between the adsorbate and the adsorbent, it is likely that the parameter values do not change much due to a phase transition
of the adsorbate, and indeed, this seems to be the case for water on graphite (Lbadaoui-Darvas et al., 2023). However, setting
125 $A_i = A_w; B_i = B_w$ would cause the melting point of an adsorbed film not to decrease below the melting point of bulk water
but to increase above it since $N_w > N_i$ for a fixed n_{H_2O} .

Although the FHH parameters cannot be exactly the same for water and ice, we can gain some insight from the derivation
by Hill (1952) of the FHH theory for Lennard-Jones (LJ) molecules. The LJ value for B depends only on the intermolecular
potential and is exactly 3. Therefore, it does not change with the solidification of LJ liquid. Likewise, A depends on the LJ
130 potential parameters, but also on the densities of the adsorbate and the adsorbent and therefore changes when a phase transition
takes place. If we make the assumption that $B_i = B_w = B$, which at least for water on graphite is not far from true (Lbadaoui-
Darvas et al., 2023), then we must have $A_i < A_w (\sigma_i/\sigma_w)^{-B}$ in order for $\Delta\mu_A$ to change sign at some temperature below
273.15 K. This can be seen when inserting Eqs. 10, 15 into Eq. 16:

$$\Delta\mu_A \approx \Delta\mu_{iw} + kT N_w^{-B} [A_i (\sigma_i/\sigma_w)^{-B} - A_w]. \quad (17)$$

135 We next derive a relation between the A -parameters of ice and water starting from an intermediate expression of Hill (1952)
for "LJ-water" and an adsorbent (subscript a) surface:

$$kT \ln S = (N_w d_w)^{-3} (C_w - C_a). \quad (18)$$

The constants C_x are given by

$$C_x = \frac{\pi \epsilon_x \zeta_x^6}{3 v_x}, \quad (19)$$

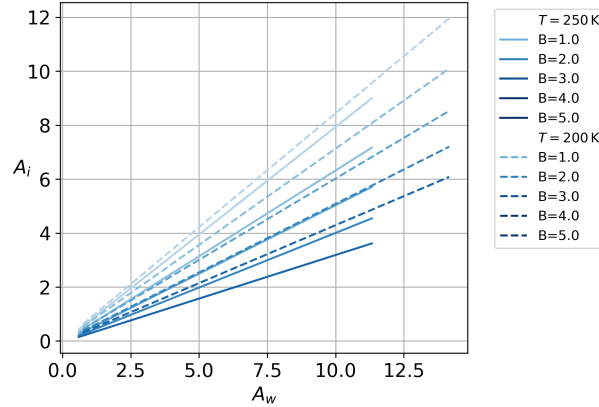


Figure 1. The variations in A_i (ice interaction) with respect to A_w (water interaction) under varying conditions of B at $T = 200$ K dashed line and $T = 250$ K solid line.

140 with ϵ_x and ς_x the LJ energy and length parameters, respectively. Rearranging and equating Eq. 18 with Eq. 2, the FHH equation (with $B = 3$) gives an expression for the FHH parameter A_w :

$$A_w = \frac{1}{kT d_w^3} (C_a - C_w) \quad (20)$$

We can now write a similar equation for A_i :

$$A_i = \frac{1}{kT d_i^3} (C_a - C_i) \quad (21)$$

145 and by eliminating the term C_a from the pair of equations and inserting Eq. 19, we get (note that the LJ parameters are the same for water and ice)

$$A_i = A_w \left(\frac{d_w}{d_i} \right)^3 + \frac{\pi \epsilon_w \varsigma_w^6}{3kT d_i^3} (v_w^{-1} - v_i^{-1}) \quad (22)$$

We next replace the exponent 3 by B (as is done to obtain the more general form of the FHH equation (Halsey, 1948; Hill, 1952)), and have

$$150 \quad A_i = A_w \left(\frac{d_w}{d_i} \right)^B + \frac{\pi \epsilon_w \varsigma_w^{2B}}{3kT d_i^B} (v_w^{-B/3} - v_i^{-B/3}). \quad (23)$$

In this way, we have reduced the number of parameters of our system from four (A_w, B_w, A_i, B_i) to two (A_w, B); in doing so we have made some approximations as the LJ potential is spherically symmetric, which is not the case with water, but at least the melting point temperature calculated with these equations seem somewhat reasonable (see section 4.1). Figure 1 shows A_i as a function of A_w at two different temperatures for B values between 1 and 5 calculated using Eq. 23. For the LJ parameters,

155 we use the following values (Kulmala, 1988): $\epsilon_w = 440.3 \cdot k$; $\varsigma_w = 0.31$ nm.



2.4 Homogeneous ice nucleation in adsorbed water

The homogeneous nucleation rate and the radius of the critical nucleus in adsorbed water are now

$$J_{hom,A} = J_{hom} \left(\frac{\Delta\mu_{iw}^2}{\Delta\mu_A^2} \right), \quad (24)$$

$$160 \quad R_{iA}^* = R_{iw}^* \left(\frac{\Delta\mu_{iw}}{\Delta\mu_A} \right). \quad (25)$$

Here we assume that all other variables except the chemical potential difference are the same for adsorbed and bulk water. The homogeneous nucleation rate of bulk water is calculated using the parameterizations for the chemical potential difference, the interfacial tension between ice and water, and the ice density (to calculate the molecular volume of ice) given by Espinosa et al. (2018) (see Appendix A2). Using these parameterizations with Eq. 8 produces nucleation rates that are in good agreement with
165 the experimental results on homogeneous freezing of water droplets. However, the parameterization of Espinosa et al. for the chemical potential difference yields a water saturation line, which differs significantly from other parameterizations found in the literature (see Murphy and Koop, 2005, and references therein). We therefore use the chemical potential difference, ice density, and ice-water interfacial tension expressions of Espinosa et al. only in calculations of the nucleation rate. In all other calculations, we use equations for the properties of water and ice given in Appendix A1.

170 The above equations hold for water films on flat surfaces, but with curved surfaces, the chemical potential should in principle be modified due to the Laplace pressure. This could be done, for example, using the equations given by Němec (2013), or by Marcolli (2020). However, we restrict our calculations to water films on relatively large particles (diameter 100 nm or more) so that the omission of the Laplace pressure effect should not produce much error.

3 Experiment

175 3.1 Substance characterization

Silica (silicon dioxide, SiO₂) powder is used in this work as a test substance for comparison of experimental deposition ice nucleation with model calculations. The powdered silica sample was prepared by grinding fused silica beads (Sigma-Aldrich, 4-20 mesh) with a planetary mill for 10 minutes at 300 rpm. For determining the particle size distribution, the powder was dry dispersed using a magnetic stirrer and a directed airflow to agitate the powder. Figure 2 shows the resulting particle size
180 distribution measured with a scanning mobility particle sizer (SMPS, 3938 TSI).

Nitrogen adsorption isotherms were measured at 77.3K with a Belsorp MAX II automatic gas adsorption instrument (Microtrac MRB). The absence of hysteresis in the nitrogen adsorption isotherm measurements (Fig. 3) indicates that the analyzed sample is non-porous.

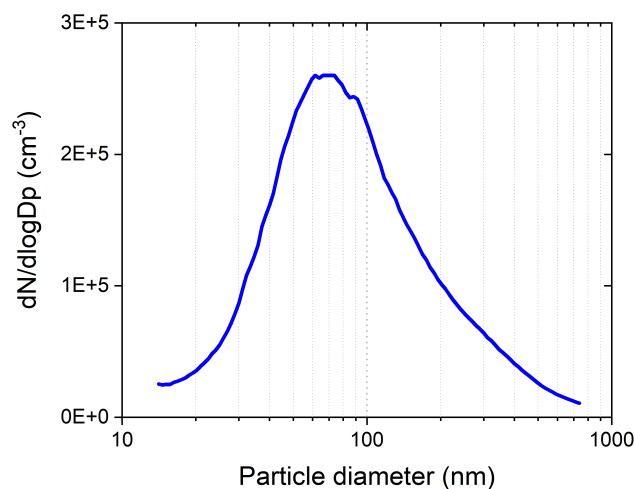


Figure 2. Size distribution of SiO₂ powder measured with a SMPS.

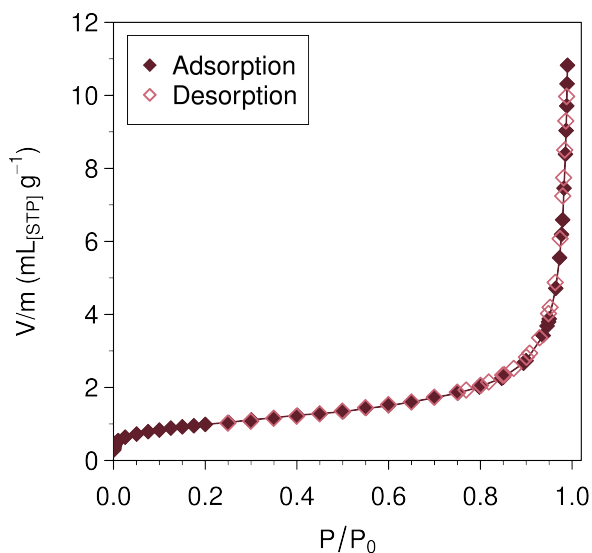


Figure 3. Nitrogen adsorption (solid symbols) and desorption (open symbols) isotherms for silica as function of nitrogen saturation ratio (P/P_0) at the boiling point of liquid nitrogen. The volume of adsorbed nitrogen is expressed per gram of sample at standard conditions.

185 3.2 SPIN measurements

Ice nucleation experiments were conducted with a modified version of the SPectrometer for Ice Nuclei (SPIN; DMT) described in Welti et al. (2020). SPIN is a continuous flow diffusion chamber-type experiment in which the test particles are exposed for a duration of approximately 10 s to constant temperature and relative humidity. The test particles were dry dispersed by agitating the powder with a magnetic stirrer in the same way as for the size distribution measurement. The concentration of



190 test particles introduced into SPIN is monitored using a condensation particle counter (CPC; Airmodus A20). Ice nucleation is
detected by the growth of ice crystals using an optical particle counter at the exit of the chamber. The ratio of ice crystals to total
particles in an experiment is reported as an activated fraction. The data points shown in this work (Section 4.4) are averaged
from three separate experimental runs into one-degree centigrade bins. The error bars are calculated as root sum squared errors
based on instrumental uncertainties of temperature and humidity, and standard deviation of the individual data points used in
195 the averaging.

4 Results and discussion

4.1 Melting point temperature

The melting point of an adsorbed ice film occurs when the chemical potential difference between the adsorbed ice and the
liquid film becomes zero. According to Eq. 16, this chemical potential difference can be expressed as $\Delta\mu_A \approx kT \ln \frac{P_w}{P_i}$. The
200 melting temperature is determined when $P_w = P_i$, as this satisfies the condition of the zero chemical potential difference. This
relationship is used to calculate the melting temperature as a function of the film thickness for each pair of A and B . Note that
in the following, we use A for A_w , and the A values shown refer to 298 K; the values of A for liquid water at other temperatures
are obtained from Eq. (4) and the A values for ice from Eq. (23).

Figure 4 illustrates the variation of vapor pressure with temperature for different interaction parameters, specifically $A = 4.0$
205 and 3.0 and $B = 1.0$ and 2.0. The liquid water film thicknesses considered are 1.5 and 3.0 nm. The intersection points of the
vapor pressure curves for water and ice, shown in Fig. 4, correspond to the melting point temperatures. The results indicate
that thicker liquid water films exhibit higher melting point temperatures compared to thinner films. Furthermore, stronger
interaction parameters (higher A , lower B) result in lower melting point temperatures.

Figure 5 illustrates the temperature of the melting point as a function of the thickness of the film for parameters A and B
210 ranging from 1.0 to 4.0. Each curve shows a clear trend where the melting point temperature increases with film thickness
before leveling off asymptotically to the bulk water melting point at higher thicknesses. Figure 5 clearly shows the impact
of the strength of the interaction between the adsorbent substrate and water, which is greater at higher values of A , and the
range of the interaction into the water layers, which is greater at lower values of B . Note that the blue curves in the two lower
panels of Fig. 5 are probably unrealistically hydrophilic compared to atmospherically relevant mineral aerosols (Kumar et al.,
215 2011). The model thus indicates that the melting point could be decreased by up to about 5 K in 1 nm thick water films on
atmospheric particles. For comparison, similar freezing-point depression is caused by five to ten weight percent of sodium
chloride in aqueous solution. Furthermore, the melting points may be reduced in films with a thickness of several nanometers
when the parameter B has values between 1 and 2. At higher values of B , the model surfaces are hydrophobic enough so that
the films must be thinner than 3 to 4 nm for any noticeable decrease in the melting point.

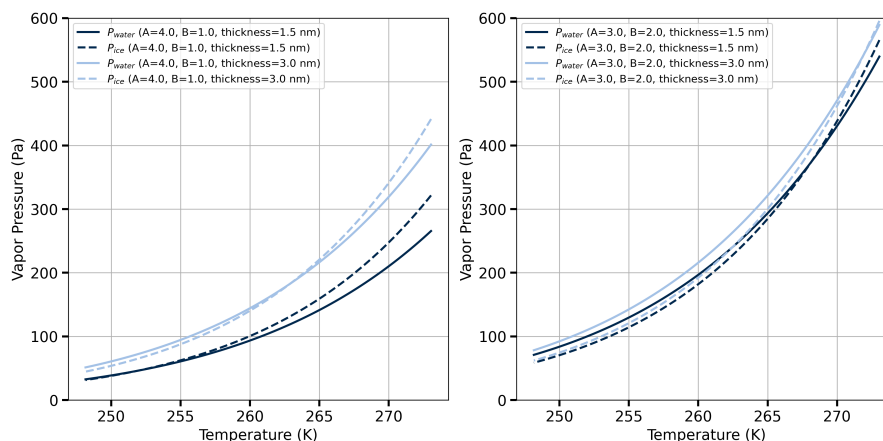


Figure 4. The figures illustrate the temperature dependent vapor pressure for adsorbed water and ice. The intersection point of the vapor pressure curves for water and ice ($\Delta\mu_A = 0$) indicates the melting point temperature. The left figure corresponds to parameter values $A = 4.0$ and $B = 1.0$, evaluated for thicknesses of 1.5 nm and 3.0 nm. The right figure shows the same analysis for $A = 3.0$ and $B = 2.0$, also evaluated for thicknesses of 1.5 nm and 3.0 nm.

220 4.2 Nucleation Rate (J)

Homogeneous nucleation rates are obtained based on Eq. 24 for different water film thicknesses and varying A and B parameters, which characterize the molecular interactions in the FHH model. The chemical potential difference $\Delta\mu_A$, present in the denominator of Eq. 24, is influenced by these A and B parameters, directly affecting nucleation rates. Furthermore, the number of water monolayers (N_w) also plays a critical role in determining $\Delta\mu_A$ and consequently the nucleation rate. The film thickness is equal to $N_w \cdot d_w$. For example, a film of 1 nm thickness consists of the equivalent of 3.5 layers of adsorbed water. The combined effect of film thickness and molecular interaction parameters is captured in the nucleation rate profile seen in Fig. 6. In both panels of Fig. 6, the nucleation rate decreases rapidly with increasing temperature, and thinner films experience more suppression of nucleation compared to thicker ones. The yellow curve, which corresponds to thinner films (1 nm), shows a much lower nucleation rate than the black curve, which represents the thicker 8 nm film. The black curves are much closer to the bulk nucleation rate, reflecting the transition from surface-controlled nucleation behavior in thin films to bulk-like behavior in thicker films. When comparing the left and right panels, it is clear that for stronger molecular interaction, represented by higher A and lower B values (right panel, $A = 4$ and $B = 1.1$), nucleation rates are generally lower across the temperature range. This suggests that increasing A while decreasing B results in stronger suppression of nucleation, particularly in thinner films. In contrast, lower A and higher B values (left panel, $A = 2.95$ and $B = 1.8$) result in higher nucleation rates, especially in thicker films. This is consistent with the molecular dynamics simulations of Hayton et al. (2024), who observed that homogeneous ice nucleation in free-standing, thin water films exhibited bulk-like behavior even at very small length scales.

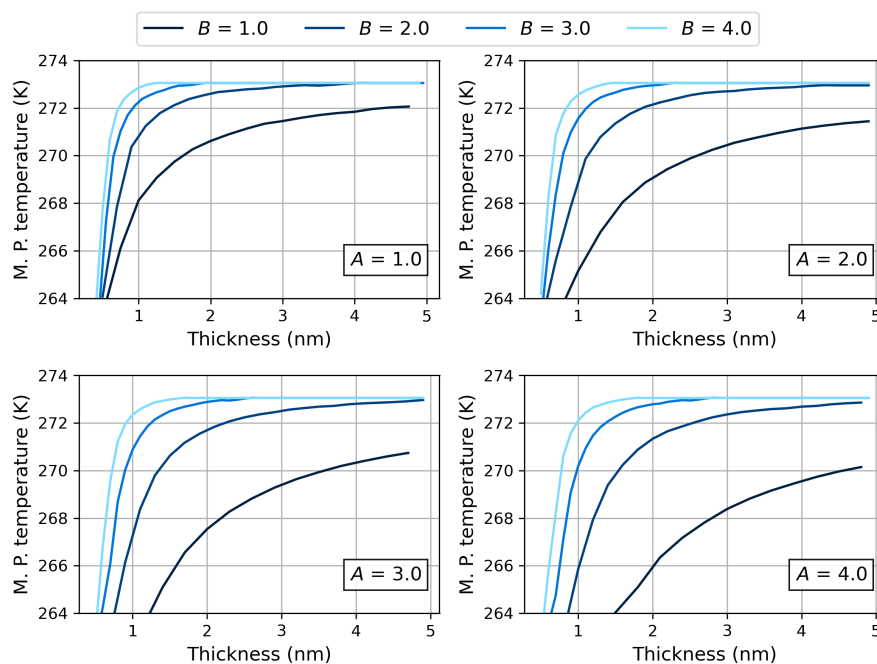


Figure 5. Melting point temperature as a function of film thickness (nm) for varying values of parameter A (1.0, 2.0, 3.0 and 4.0) and parameter B (1.0, 2.0, 3.0 and 4.0). The four panels show the influence of increasing A on the melting point. The effect of different B values is shown in each panel with higher B values generally leading to less melting point depression across all thicknesses.

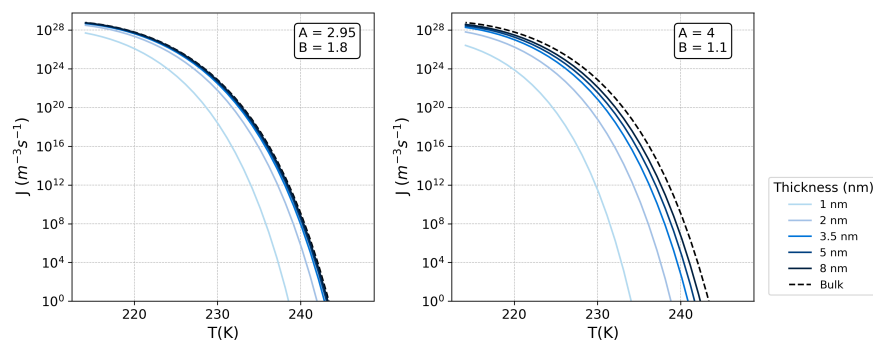


Figure 6. Comparison of nucleation rates (J ($\text{m}^{-3}\text{s}^{-1}$)) as a function of temperature (T) for different parameter sets. The left panel shows results for systems with $A = 2.95$ and $B = 1.8$, while the right panel displays results for $A = 4$ and $B = 1.1$. Each curve corresponds to nucleation rates under different film thicknesses ranging from 1 nm to 8 nm and a bulk system case (dashed line). The nucleation rate is presented on a logarithmic scale.

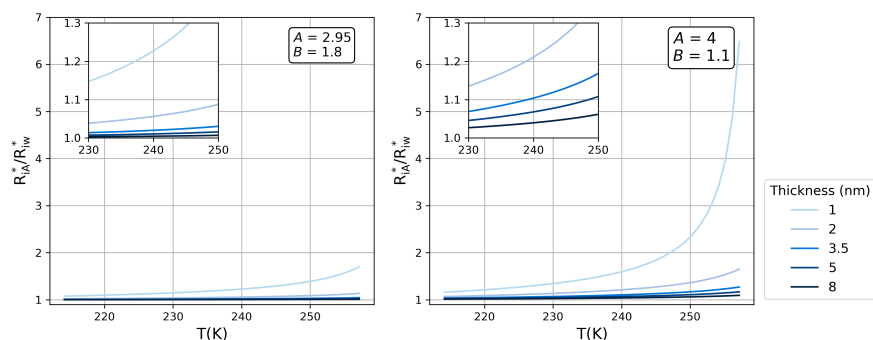


Figure 7. The ratio R_{iA}^*/R_{iw}^* , representing the radius of critical nucleus in adsorbed water (R_{iA}^*) to the radius of the critical nucleus in a homogeneous case (R_{iw}^*) as a function of temperature $T(K)$. Note that according to Eq. 25: $R_{iA}^*/R_{iw}^* = \Delta\mu_{iw}/\Delta\mu_A$. The curves correspond to different values of parameters A , B (FHH isotherm) and film thicknesses. The zoomed-in insets highlight the behavior in the temperature range from 230 K to 250 K. The results show that smaller film thicknesses lead to a more pronounced increase in the critical nucleus size ratio as temperature rises, indicating greater sensitivity to temperature changes in systems with thinner adsorbed water layers.

4.3 Critical radius

The radius of the critical nucleus in the adsorbed water film and the bulk water is calculated using Eq. 25 and Eq. 9, respectively. The ratio of these radii is shown in Fig. 7 for different A and B and thicknesses of the water film. The left panel of Fig. 7 shows the results for $A = 2.95$, $B = 1.8$, while the right panel corresponds to $A = 4$, $B = 1.1$, covering a range of film thicknesses from 1 to 8 nm. In both panels, the thinner water films exhibit a higher ratio of critical nucleus radii compared to thicker films, especially at lower temperatures. For example, the 1 and 2 nm films, show significantly larger ratios compared to the other curves, indicating that the critical nucleus radius in adsorbed water becomes notably larger than in bulk water for thinner films. This suggests that for thin films, adsorption has a stronger effect on suppressing nucleation by increasing the critical nucleus size. The inset zooms in on the temperature range between 230 K and 250 K to highlight the behavior near the onset of homogeneous freezing. In both panels, the ratio of critical radii approaches unity at lower temperatures, particularly for thicker films (5 and 8 nm). Figs. 6 and 7 indicate that for thicker films, the nucleation behavior of adsorbed water films becomes increasingly similar to that of the bulk water, especially below the onset temperature of homogeneous freezing around 235 K. The right panel, with $A = 4$ and $B = 1.1$, shows a higher increase in the critical radius ratio at lower temperatures, suggesting that higher interaction values (larger A , smaller B) cause a greater deviation from the nucleation behavior of bulk water.

4.4 Critical supersaturations for ice nucleation

Figure 8 shows the variation of critical supersaturation with respect to ice (given as relative humidity RH_{ice}^*) as a function of temperature, calculated using two different expressions for equilibrium vapor pressure over water. In the left panel, the equilibrium vapor pressure is calculated using the equation of Murphy and Koop (2005). The panel on the right uses the expression for the equilibrium water vapor pressure given by Wagner and Pruss (2002). Both equations are given in Appendix A1. Above

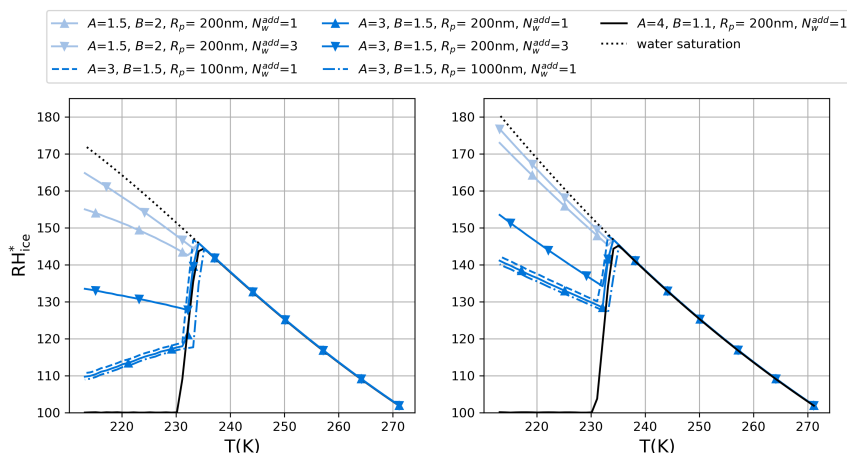


Figure 8. Comparison of critical relative humidity with respect to ice (RH_{ice}^*) as a function of temperature (T) for different parameter sets. The left plot uses the water saturation model from Murphy and Koop (2005), while the right plot applies the expression for equilibrium water vapor pressure given by Wagner and Pruss (2002). Each line represents different combinations of parameters A , B , and number of additional water monolayers (N_w^{add}) separating the critical nucleus from the adjacent surface or the vapor phase. The dashed lines show the sensitivity to particle radius (R_p).

235 K, the vapor pressures obtained from these two expressions are almost equal, but they deviate at lower temperatures, in the "no man's land" where vapor pressures of supercooled water cannot be measured directly. In our calculations, we assume adsorbed water to be frozen when the nucleation probability

$$P = 1 - \exp(-J_{hom,A} V_A \tau) \geq 0.01 \quad (26)$$

260 where V_A denotes the volume of adsorbed water on a single ice nucleus, and the time τ is taken to be equal to the residence time in the SPIN instrument which is 10 s. The criterion represented by Eq. 26 corresponds to a one percent activated fraction of aerosols as measured by SPIN. Figure 8 displays several curves corresponding to different parameterizations of the FHH adsorption model, which describes multilayer adsorption of water onto a substrate. Ice nucleation is likely to occur homogeneously rather than heterogeneously on surfaces that can induce ice premelting (Qiu and Molinero, 2018). Surface adjacent
 265 water can be strongly bound to the substrate and can thereby be hindered to rearrange into an ice like lattice structure (Barahona, 2018, and references therein). On such surfaces, there will be at least one layer of liquid-like water between the surface and the critical ice nucleus. Furthermore, one or more liquid-like layers could separate the ice nucleus from the vapor phase. To test the influence of additional layers not involved in the formation of the critical nucleus, we require that the thickness of the adsorbed layer has to be equal to the diameter of the critical ice nucleus plus one to three monolayers of water for ice nucleation
 270 to become possible. The number of additional monolayers is indicated by N_w^{add} in the legend of Fig. 8. The FHH parameters A and B , and the number of additional monolayers (N_w^{add}) separating the critical nucleus from the substrate or surrounding vapor



phase vary between the curves, and these differences affect the supersaturation required for ice nucleation. The black dotted line in both panels of Fig. 8 represents the water saturation line, indicating the RH_{ice} at which water condenses. Initially, as the temperature decreases, the criterion of Eq. 26 is not fulfilled below water saturation. The temperature at which freezing occurs is seen as a steep drop off in the relative humidity (RH_{ice}^*) line from the water saturation line. There is some variation in the exact temperature at which the separation of the critical supersaturation RH_{ice}^* from the water saturation line occurs, which is due to the variability of the nucleation rate and the adsorbed volume between the different FHH models at a given temperature and humidity. However, as the nucleation rate increases very steeply in the vicinity of 233 K, the variation of the separation temperature remains quite small. Once the separation of the RH_{ice}^* from the water saturation line has occurred, the lines level off or start increasing again. These turns are caused by two different limiting factors. First, the thickness of the adsorbed water film must be large enough to accommodate the critical ice nucleus plus N_w^{add} . If the critical nucleus size did not change with temperature, the curves would be parallel to the water saturation line because the amount of adsorbed water is almost constant at a fixed relative humidity (with respect to liquid water) within a temperature range of 10-20 degrees. However, the size of the critical nucleus decreases with temperature, bending the curves away from the water saturation line. Second, with the curves leveling off very close to ice saturation, the limiting factor is not the thickness of the adsorbed layer, as in these cases, the adsorbed layer is thick enough to accommodate the critical ice nucleus already below ice saturation. Rather, the limitation in these cases is similar to that in the activation of insoluble CCN to cloud droplets (Sorjamaa and Laaksonen, 2007); the ice particle must overcome a Köhler-type maximum created by competition between the FHH and Kelvin terms (cf. Eq. 6 for ice adsorption) for rapid growth to ensue. In other words, ice clusters can only grow freely in ice supersaturated conditions.

290 4.5 Comparison of theory and experiment

Figure 9 compares the results of our model calculations with the experimental data for silica (SiO_2). We chose silica as the ice nucleating material because it is likely that heterogeneous freezing does not occur on premelting inducing silica surfaces (David et al., 2019). As seen in Fig. 9, several research groups have measured ice nucleation on silicas, and there is quite a lot of variability among the results. In addition to experimental errors, we believe that an important reason for the scatter of the results is the large physical and chemical variability of different types of silicas. Silica can be either crystalline or amorphous and porous or non-porous. The surface chemistry of silica varies depending on how it has been manufactured and whether it has been treated thermally (calcinated) and/or hydrated. Bare silica surfaces are rather hydrophobic, but contact with water induces the formation of surface silanol ($SiOH$), siloxide (SiO^-) and siloxane ($Si-O-Si$) groups. Silanol and siloxide are hydrophilic, whereas siloxane is hydrophobic. For example, silicas produced chemically from solutions of low pH and calcinated silicas tend to be hydrophobic (Warring et al., 2016). The predictions of the model of RH_{ice}^* as a function of temperature, shown as different lines, were generated using varying values of A and B , corresponding to different interaction strengths, as well as two to four additional layers N_w^{add} of surface adjacent water, or layers at the liquid-vapor interphase that do not participate in ice nucleation. The experimental data shown in pink and green represent literature data, while the black data represent the experimental results of our laboratory. It should be mentioned that the silica particle sizes are variable, whereas in our model calculations, we set the particle size to 400 nm. The size distribution of the silica used in our experiments (Fig. 2) peaks at

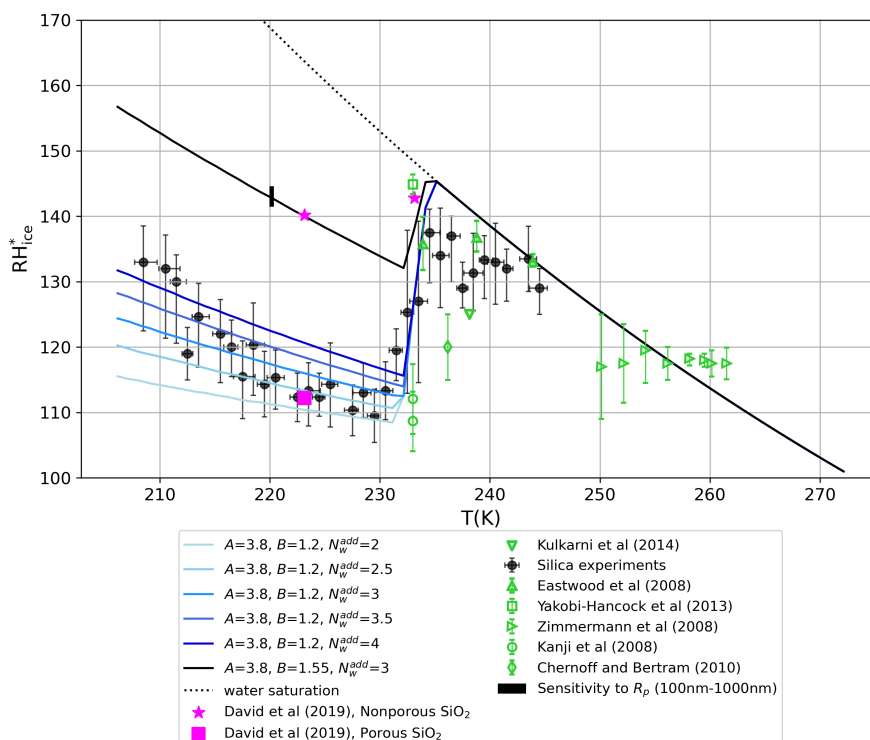


Figure 9. Comparison of relative humidity with respect to ice (RH_{ice}) as a function of temperature (T) for various experimental studies and model outputs. The water saturation curve was calculated using the expression for equilibrium vapor pressure given by Wagner and Pruss (2002). The vertical bar on the red curve reflects the theoretical model’s sensitivity of RH_{ice} to particle radius (R_p from 100 nm to 1000 nm). Error bars on the data points indicate experimental uncertainties reported in the respective studies.

about 70 nm; however, it is unlikely that particles smaller than 100 nm have contributed to the 1 % activated fraction. Above 100 nm, the model size dependence is quite weak; the vertical bar in Fig. 9 indicates how much the critical supersaturation lines would shift up if the particle size was 100 nm and down if the particle size was 1000 nm (see also solid green curves in Fig. 8). According to the model, 50 nm particles with the same FHH parameters would nucleate ice at $RH_{ice}^* = 151\%$. The model lines
 310 generated with our model fit the experimental data (black circles) very well, suggesting that the model accurately captures the RH_{ice}^* behavior of silica particles over a range of temperatures, especially at temperatures below 235 K. Zimmermann et al. (2008) reported the temperature of ice formation and the corresponding supersaturation for the deposition ice nucleation on silica particles at 250–265 K, which is represented by green right triangles in Fig. 9. They found almost constant RH_{ice}^* of 117%; however, the error bars of the data points extend to the water saturation line. In the study by Eastwood et al. (2008), the onset
 315 conditions of deposition ice nucleation for quartz at 233 – 246 K is reported to occur close to water saturation, as indicated by green up triangles. The onset humidity conditions of Kanji et al. (2008) at 233 K are close to our model predictions, while those



of Yakobi-Hancock et al. (2013) and Chernoff and Bertram (2010) appear to part from the water saturation line at temperatures a few degrees warmer than our model prediction. The pink square and two stars indicate the experimental data of David et al. (2019), representing data for porous silica and for non-porous silica, respectively. Interestingly, the data point for porous silica coincides with our own experiments and with model predictions for hydrophilic silica with the FHH parameters $A = 3.8$ and $B = 1.2$, while the data points for non-porous silica correspond to model prediction for more hydrophobic silica with $A = 3.8$ and $B = 1.55$. For comparison, Kumar et al. (2011) obtained $A = 2.95$, $B = 1.36$ from CCN activation experiments with silica particles. Our interpretation is that the calcinated silicas used by David et al. (2019) are hydrophobic and the non-calcinated silica used in our experiments is hydrophilic. If experiments were performed for silica that is as hydrophilic as that used in our experiments but also porous, the resulting critical supersaturations would likely be below that of the data point (pink square) of David et al. (2019)

An important factor in the promising agreement of our model with the experimental data, especially at lower temperatures (below 235 K), is the incorporation of the equilibrium vapor pressure equation derived by Wagner and Pruss (2002). This equation improved the performance of our model relative to the vapor pressure equation of Murphy and Koop (2005) by making the critical supersaturation curves steeper (see Fig. 8).

5 Conclusions

In this study, we extended the FHH adsorption theory to model the homogeneous ice nucleation in supercooled water films adsorbed on insoluble substrates. We derived theoretical equations for the chemical potential in adsorbed water that allow for the prediction of homogeneous ice nucleation on the basis of classical nucleation theory. Our theoretical approach captures the complex relationship between molecular interactions, described by the FHH parameters A and B , and the thickness of the film in determining the conditions of ice nucleation. We showed that the melting point, critical nucleus size, and nucleation rates are influenced by the thickness of the water film, with thinner films exhibiting the largest effects on the conditions for ice nucleation because of stronger adsorbate substrate interactions. The model was validated against experimental data for silica particles. The critical relative humidity with respect to ice (RH_{ice}^*) predicted for the onset of nucleation as a function of temperatures agrees well with both our laboratory results and previous studies. It should be noted that the equilibrium vapor pressure equation derived by Wagner and Pruss (2002) improved the agreement with the experimental data, especially at temperatures below 235 K. These findings emphasize the importance of the adsorption of a multilayer water film in deposition ice nucleation process on insoluble aerosols in the atmosphere. By providing a detailed description of how ice nucleation in these systems varies with film thickness and substrate interactions, this work offers insights into ice cloud formation. Future studies could explore refinements of the FHH model to include additional complexities, such as the impact of surface curvature and chemical heterogeneity, or use the model to describe heterogeneous freezing within adsorbed water films.



Code and data availability. The model code used for analysis as well as ice nucleation and adsorption data from this work are available upon request from the authors.

Author contributions. AL developed the theory, GR conducted the calculations, performed adsorption measurements, AW conducted ice nucleation experiments. AL and GR wrote the manuscript. All authors commented the manuscript. AL acquired funding and supervised the project.

Competing interests. A.L. is a member of the editorial board of Atmospheric Chemistry and Physics.

Acknowledgements. This work was supported by the Academy of Finland Flagship ACCC (grant no. 337552) and MEDICEN project (grant no. 345125).



355 Appendix A: Parametrisations used in the computations

A1 Water and ice properties

T denotes absolute temperature (K) and T_c is the temperature in degrees centigrade.

Density of liquid water (Marcolli, 2017) (g cm^{-3}):

$$\begin{aligned} \rho_w = & 1.8643535 - 0.0725821489T + 2.5194368 \cdot 10^{-3}T^2 \\ & + 4.9000203 \cdot 10^{-5}T^3 + 5.860253 \cdot 10^{-7}T^4 - 4.5055151 \cdot 10^{-9}T^5 \\ & + 2.2616353 \cdot 10^{-11}T^6 - 7.3484974 \cdot 10^{-14}T^7 + 1.4862784 \cdot 10^{-16}T^8 \\ & - 1.6984748 \cdot 10^{-19}T^9 + 8.3699379 \cdot 10^{-23}T^{10} \end{aligned}$$

360 Density of ice (Pruppacher and Klett, 1997) (kg m^{-3}):

$$\rho_i = 916.7 - 0.175T_c - 0.0005T_c^2$$

The molecular volumes of water and ice are given by

$$v_w(T) = \frac{M_w}{\rho_w(T)N_A}$$

and

$$365 \quad v_i(T) = \frac{M_w}{\rho_i(T)N_A},$$

with M_w the molecular mass of water, and N_A Avogadro's number.

Equilibrium vapor pressure of liquid water (Murphy and Koop, 2005) (Pa):

$$\begin{aligned} e_w = & \exp[54.842763 - 6763.22/T - 4.21 \ln(T) + 0.000367T \\ & + \tanh[0.0415(T - 218.8)][53.878 - 1331.22/T \\ & - 9.44523 \ln(T) + 0.014025T]] \end{aligned}$$

Equilibrium vapor pressure of liquid water (Wagner and Pruss, 2002) (Pa):

$$370 \quad e_w = P_c \exp[T_c T^{-1}(-7.85951783\tau + 1.84408259\tau^{1.5} - 11.7866497\tau^3 \\ + 22.6807411\tau^{3.5} - 15.9618719\tau^4 + 1.80122502\tau^{7.5})]$$

Here $\tau = 1 - TT_c^{-1}$ and the critical temperature and pressure are $T_c = 647.096$ K and $P_c = 22.064$ MPa.

Equilibrium vapor pressure of hexagonal ice (Murphy and Koop, 2005) (Pa) :

$$e_i = \exp[9.550426 - 5723.265/T + 3.53068 \ln(T) - 0.00728332T]$$



Surface tension of water(Hrubý et al., 2014) (N/m):

375 $\gamma_w = 0.2358(1 - T/647.096)^{1.256}[1 - 0.625(1 - T/647.096)]$

Interfacial tension between liquid water and hexagonal ice (N/m) is calculated using the Antonoff rule:

$$\gamma_{iw} = \gamma_i - \gamma_w,$$

where the ice-vapor interfacial tension is obtained from

$$\gamma_i = 0.1364 - 0.00015T.$$

380 This relation, with the temperature dependence of Hale and Plummer (1974), returns the experimental value of 0.98 N/m at 255.85 K (Boinovich and Emelyanenko, 2014)

A2 Parametrizations used in nucleation rate calculations

Pre-exponential factor of nucleation rate of ice in bulk water (Espinosa et al., 2018) ($\text{m}^{-3}\text{s}^{-1}$):

$$C = \exp(91.656 + 0.11729T_c + 0.00081401T_c^2)$$

385 Chemical potential difference between water and ice used in calculation of nucleation rate (Espinosa et al., 2018) (J/mol):

$$\Delta\mu_{iw}(0.00035032 - 0.0046013T_c - 2.3187 \cdot 10^{-5}T_c^2 + 6.9536 \cdot 10^{-8}T_c^3)/4184$$

Density of hexagonal ice used in calculation of nucleation rate (Espinosa et al., 2018) (g cm^{-3}):

$$\rho_i = 0.906 - 0.14 \cdot 10^{-3}T_c$$

Interfacial tension between liquid water and hexagonal ice used in calculation of nucleation rate (Espinosa et al., 2018) (N/m):

390 $\gamma_{iw} = (29.986 + 0.25559T_c - 0.0010465T_c^2 - 4.6503 \cdot 10^{-6}T_c^3 + 2.9065 \cdot 10^{-7}T_c^4)/1000.$



References

- Barahona, D.: On the thermodynamic and kinetic aspects of immersion ice nucleation, *Atmospheric Chemistry and Physics*, 18, 17 119–17 141, <https://doi.org/10.5194/acp-18-17119-2018>, 2018.
- Boinovich, L. B. and Emelyanenko, A. M.: Experimental determination of the surface energy of polycrystalline ice, *Doklady Phys. Chem.*, 395 459, 702–706, 2014.
- Chernoff, D. I. and Bertram, A. K.: Effects of sulfate coatings on the ice nucleation properties of a biological ice nucleus and several types of minerals, *J. Geophys. Res.*, 115, D20 205, <https://doi.org/10.1029/2010JD014254>, 2010.
- David, R. O., Marcolli, C., Fahrni, J., Qiu, Y., Perez Sirkin, Y. A., Molinero, V., Mahrt, F., Brühwiler, D., Lohmann, U., and Kanji, Z. A.: Pore condensation and freezing is responsible for ice formation below water saturation for porous particles, *Proc. Natl. Acad. Sci. U. S. A.*, 116, 8184–8189, <https://doi.org/10.1073/pnas.1813647116>, 2019.
- Eastwood, M. L., Cremel, S., Gehrke, C., Girard, E., and Bertram, A. K.: Ice nucleation on mineral dust particles: Onset conditions, nucleation rates and contact angles, *J. Geophys. Res.*, 113, D22 203, <https://doi.org/10.1029/2008JD010639>, 2008.
- Espinosa, J. R., Vega, C., and Sanz, E.: Homogeneous ice nucleation rate in water droplets, *J. Phys. Chem. C*, 122, 22 892–22 896, <https://doi.org/10.1021/acs.jpcc.8b04788>, 2018.
- 405 Fletcher, N. H.: On ice-crystal production by aerosol particles, *J. Atmos. Sci.*, 16, 173–180, [https://doi.org/10.1175/1520-0469\(1959\)016<0173:OICPBA>2.0.CO;2](https://doi.org/10.1175/1520-0469(1959)016<0173:OICPBA>2.0.CO;2), 1959.
- Fortes, A. D.: Accurate and precise lattice parameters of H₂O and D₂O ice *Ih* between 1.6 and 270K from high-resolution time-of-flight neutron powder diffraction data, *Acta Crystallographica Section B*, 74, 196–216, <https://doi.org/10.1107/S2052520618002159>, 2018.
- Frenkel, J.: *Kinetic Theory of Liquids*, Oxford University Press, London, 1946.
- 410 Haji-Akbari, A. and Debenedetti, P. G.: Computational investigation of surface freezing in a molecular model of water, *Proc. Natl. Acad. Sci. U. S. A.*, 114, 3316–3321, <https://doi.org/10.1073/pnas.1620999114>, 2017.
- Haji-Akbari, A., DeFever, R. S., Sarupia, S., and Debenedetti, P. G.: Suppression of sub-surface freezing in free-standing thin films of a coarse-grained model of water, *Phys. Chem. Chem. Phys.*, 16, 25 916–25 927, <https://doi.org/10.1039/C4CP03948C>, 2014.
- Hale, B. N. and Plummer, P. L. M.: Molecular model for ice clusters in a supersaturated vapor, *J. Chem. Phys.*, 61, 4012–4019, 1974.
- 415 Halsey, G.: Physical Adsorption on Non-Uniform Surfaces, *J. Chem. Phys.*, 16, 931–937, <https://doi.org/10.1063/1.1746689>, 1948.
- Hayton, J. A., Davies, M. P., Whale, T. F., Michaelides, A., and Cox, S. J.: The limit of macroscopic homogeneous ice nucleation at the nanoscale, *Faraday Discuss.*, 249, 210–218, <https://doi.org/10.1039/d3fd00099k>, 2024.
- Hill, T. L.: Theory of Physical Adsorption, *Adv. Catal.*, 4, 211–258, [https://doi.org/10.1016/S0360-0564\(08\)60615-X](https://doi.org/10.1016/S0360-0564(08)60615-X), 1952.
- Hrubý, J., Vinš, V., Mareš, R., and Kalová, J.: Surface tension of supercooled water: no inflection point down to –25 °C, *J. Phys. Chem. Lett.*, 5, 425–428, 2014.
- 420 Kanagy, J. R.: Influence of temperature on the adsorption of water vapor by collagen and leather, *J. Res. NBS*, 44, 31–45, 1950.
- Kanji, Z. A., Florea, O., and Abbatt, J. P. D.: Ice formation via deposition nucleation on mineral dust and organics: dependence of onset relative humidity on total particulate surface area, *Environ. Res. Lett.*, 3, 025 004, <https://doi.org/10.1088/1748-9326/3/2/025004>, 2008.
- Kulmala, M.: Nucleation as an aerosol physical problem, Ph.D. thesis, University of Helsinki, 1988.
- 425 Kumar, P., Sokolik, I. N., and A., N.: Measurements of cloud condensation nuclei activity and droplet activation kinetics of fresh unprocessed regional dust samples and minerals, *Atmos. Chem. Phys.*, 11, 3527–3541, <https://doi.org/10.5194/acp-11-3527-2011>, 2011.



- Laaksonen, A.: A Unifying Model for Adsorption and Nucleation of Vapors on Solid Surfaces, *J. Phys. Chem. A*, 119, 3736–3745, <https://doi.org/10.1021/acs.jpca.5b00325>, 2015.
- Laaksonen, A. and Malila, J.: Homogeneous gas–liquid nucleation theory, in: *Nucleation of Water: From Fundamental Science to Atmospheric and Additional Applications*, Elsevier, Amsterdam, <https://doi.org/10.1016/B978-0-12-814321-6.00012-9>, 2021.
- Laaksonen, A., Malila, J., and Nenes, A.: Heterogeneous nucleation of water vapor on different types of black carbon particles, *Atmospheric Chemistry and Physics*, 20, 13 579–13 589, <https://doi.org/10.5194/acp-20-13579-2020>, 2020.
- Lbadaoui-Darvas, M., Laaksonen, A., and Nenes, A.: Deposition freezing, pore condensation freezing and adsorption: three processes, one description?, *Atmos Chem. Phys.*, 23, 10 057–10 074, <https://doi.org/10.5194/acp-23-10057-2023>, 2023.
- Lü, Y., Zhang, X., and Chen, M.: Size effect on nucleation rate for homogeneous crystallization of nanoscale water film, *J. Phys. Chem. B*, 117, 10 241–10 249, <https://doi.org/10.1021/jp404403k>, 2013.
- Marcolli, C.: Deposition nucleation viewed as homogeneous or immersion freezing in pores and cavities, *Atmospheric Chemistry and Physics*, 14, 2071–2104, <https://doi.org/10.5194/acp-14-2071-2014>, 2014.
- Marcolli, C.: Pre-activation of aerosol particles by ice preserved in pores, *Atmos. Chem. Phys.*, 17, 1595–1622, 2017.
- Marcolli, C.: Technical note: Fundamental aspects of ice nucleation via pore condensation and freezing including Laplace pressure and growth into macroscopic ice, *Atmos Chem. Phys.*, 20, 3209–3230, <https://doi.org/10.5194/acp-20-3209-2020>, 2020.
- McClellan, A. L. and Harnsberger, H. F.: Cross-sectional areas of molecules adsorbed on solid surfaces, *J. Colloid Interface Sci.*, 23, 577–599, 1967.
- Murphy, D. M. and Koop, T.: Review of the vapour pressures of ice and supercooled water for atmospheric applications, *Q. J. R. Meteorol. Soc.*, 131, 1539–1565, 2005.
- Němec, T.: Estimation of ice–water interfacial energy based on pressure-dependent formulation of classical nucleation theory, *Chem. Phys. Lett.*, 583, 64–68, <https://doi.org/10.1016/j.cplett.2013.07.085>, 2013.
- Pruppacher, H. and Klett, J.: *Microphysics of clouds and precipitation*, Reidel, Dordrecht, 1997.
- Qiu, Y. and Molinero, V.: Why is it so difficult to identify the onset of ice premelting?, *J. Phys. Chem.*, 9, 5179–5182, 2018.
- Roudsari, G., Lbadaoui-Darvas, M., Welti, A., Nenes, A., and Laaksonen, A.: The molecular scale mechanism of deposition ice nucleation on silver iodide, *Environ. Sci. Atmos.*, 4, 243–251, <https://doi.org/10.1039/D3EA00140G>, 2024.
- Sorjamaa, R. and Laaksonen, A.: The effect of H₂O adsorption on cloud drop activation of insoluble particles: a theoretical framework, *Atmos Chem. Phys.*, 7, 6175–6180, <https://doi.org/10.5194/acp-7-6175-2007>, 2007.
- Wagner, W. and Pruss, A.: The IAPWS formulation 1995 for the thermodynamic properties of ordinary water substance for general and scientific use, *J. Phys. Chem. Ref. Data*, 31, 387–535, 2002.
- Warring, S. L., Beate, D. A., and McQuillan, J.: Surficial siloxane-to-silanol interconversion during room-temperature hydration/dehydration of amorphous silica films observed by ATR-IR and TIR-Raman spectroscopy, *Langmuir*, 32, 1568–1576, 2016.
- Welti, A., Kanji, Z. A., Lüönd, F., Stetzer, O., and Lohmann, U.: Exploring the Mechanisms of Ice Nucleation on Kaolinite: From Deposition Nucleation to Condensation Freezing, *Journal of the Atmospheric Sciences*, 71, 16 – 36, <https://doi.org/10.1175/JAS-D-12-0252.1>, 2014.
- Welti, A., Korhonen, K., Miettinen, P., Piedehierro, A. A., Viisanen, Y., Virtanen, A., and Laaksonen, A.: SPIN modification for low-temperature experiments, *Atmospheric Measurement Techniques*, 13, 7059–7067, <https://doi.org/10.5194/amt-13-7059-2020>, 2020.
- Yakobi-Hancock, J. D., Ladino, L. A., and Abbatt, J. P. D.: Feldspar minerals as efficient deposition ice nuclei, *Atmos Chem. Phys.*, 13, 11 175–11 185, <https://doi.org/10.5194/acp-13-11175-2013>, 2013.

<https://doi.org/10.5194/egusphere-2024-4095>

Preprint. Discussion started: 15 January 2025

© Author(s) 2025. CC BY 4.0 License.



Zimmermann, F., Weinbruch, S., Schütz, L., Hofmann, H., Ebert, M., Kandler, K., and Worringer, A.: Ice nucleation properties of the most
465 abundant mineral dust phases, *J. Geophys. Res.*, 113, D23 204, <https://doi.org/10.1029/2008JD010655>, 2008.